

Raman spectrum of $1T'$ -WTe₂ under tensile strain: A first-principles prediction

Wei Yang,^{1,*} Zi-Yang Yuan,¹ Ying-Qi Luo,¹ Yu Yang,² Fa-Wei Zheng,²
Zong-Hai Hu,¹ Xiao-Hui Wang,¹ Yuan-An Liu,¹ and Ping Zhang^{2,3,†}

¹*Beijing Key Laboratory of Work Safety Intelligent Monitoring,
Beijing University of Posts and Telecommunications,
Beijing 100876, People's Republic of China*

²*Institute of Applied Physics and Computational Mathematics,
Beijing 100088, People's Republic of China*

³*Beijing Computational Science Research Center,
Beijing 100084, People's Republic of China*

Abstract

Monolayer WTe₂ attracts rapidly growing interests for its large-gap quantum spin Hall effect, which enables promising applications in flexible logic devices. Due to one-dimensional W - W chains, $1T'$ -WTe₂ exhibits unique anisotropic structure and promising properties, which can be modified by simply applying strains. Based on the first-principles simulations, we show that phonon branch undergoes soft down to negative frequency at special q points under different critical strains, *i.e.*, $\varepsilon_a = 11.55\%$ along a -axis (with W - W chains) direction, $\varepsilon_b = 7.0\%$ along b -axis direction and $\varepsilon_{ab} = 8.44\%$ along biaxial direction. Before each critical strain, the Raman-shift of A_g^1 , A_g^3 and A_g^4 modes, corresponding to the main peaks in Raman spectra of $1T'$ -WTe₂, shows anisotropic response to uniaxial strain but most sensitive to biaxial strain. Interestingly, we find that the frequency shift of A_g^3 mode show parabolic characters of strained $1T'$ -WTe₂, then we split it into two parts and it shows a Raman-shift transition at $\sim 5\%$ strains. While for the A_g^1 and A_g^4 modes, the frequencies change linearly. Through careful structure and vibration analysis, we try to explain these Raman irregularity in strained $1T'$ -WTe₂.

PACS numbers: 63.20.D-, 63.22.-m

*Author to whom correspondence should be addressed. Electronic mail: yangwei@bupt.edu.cn

†Author to whom correspondence should be addressed. Electronic mail: zhang_ping@iapcm.ac.cn

I. INTRODUCTION

In a robust two-dimensional materials family of transition metal dichalcogenides (TMDs) [1], monolayer $1T'$ -WTe₂ has large-gap quantum spin Hall (QSH) insulator [2–11], unconventional spin-torque [12] and gate-tunable superconductivity [13], which attracts rapidly growing interests, and enable promising applications in spintronics, dissipationless transport, and quantum computations. Among $1T'$ -TMDs—MX₂ with M = (W, Mo) and X = (Te, Se, S)—theoretically predicted to be a new class of QSH insulators [2], WTe₂ is the only one for which the $1T'$ phase is most energetically favoured [2] and can be observed under ambient conditions [1, 14]. $1T'$ -WTe₂ with a distorted orthorhombic crystal structure is distinct anisotropy in contrast to the other monolayer TMDs crystallized in $1H$ (trigonal prismatic coordination) or $1T$ (octahedral coordination) structures. In plane, the covalently bonded W atoms form a zigzag W - W chain, which makes WTe₂ structurally one-dimensional and electronically a semimetal [15]. When cutting $1T'$ -WTe₂ into nanoribbons perpendicular to the W - W chains in our previous study [16], the electronic band opens a gap, and semimetal transforms to semiconductor. Other theoretical studies also found that only 1% tensile strain along the W - W chains can lead to a semimetal to semiconductor or QSH insulator transition [17, 18]. Moreover, the Poisson ration, the in-plane stiffness and the absorption spectrum of monolayer $1T'$ -WTe₂ are strongly dependent on and tunable by tensile strain [17].

Strain engineering in different orientations can lead to anisotropic modifications to the structure and properties of monolayer $1T'$ -WTe₂, which could play important roles in the application of flexible logic devices [19]. Theoretical and experimental studies on graphene [20, 21], monolayer h -BN [22, 23] and $1H$ -MX₂ with M = (W, Mo) and X = (Se, S) [24–29] have found that the phonon spectra are significantly affected by external strains, and their response can be probed by Raman spectroscopy [30]. In contrast to these $1H$ structures with in-plane isotropic, $1T'$ -WTe₂ under strain would exhibit more interesting anisotropic properties. The Raman spectrum of WTe₂, from monolayer, few-layer to bulk as well as alloys [31–40], has been studied to detect the crystal structure, lattice vibration, number of layers and in-plane anisotropy, however, the Raman spectrum of strained WTe₂ has not yet been studied by either theory or experiment.

Based on the first-principles calculations, we provide a thorough study on the changes

of structures, phonon spectra, and Raman-active modes of monolayer $1T'$ -WTe₂ under uniaxial (parallel or perpendicular to the W - W chains, respectively) and equibiaxial tensile strains. Here, we only focus on $1T'$ -WTe₂ under tension since a $1T'$ - $1H$ phase transition will occur under compression [41], which may be experimentally challenging to achieve without incurring any buckling response. Through our phonon dispersion curve calculations, we find that the acoustic branches of phonon are the most sensitive to tensile strains, and a soft mode with negative frequency at different q point under different critical strain occurs, which indicate the structural instability and signify the ideal strength of $1T'$ -WTe₂ withstanding larger strain before rupture. Besides, we also find that the Raman-active modes response quite different to external strains, and their corresponding frequency changes are anisotropic. These results indicate that Raman measurements are sufficient to detect the strain magnitudes and structural stability of $1T'$ -WTe₂.

II. COMPUTATIONAL METHOD

Our calculations are based on density functional theory (DFT) and density functional perturbation theory (DFPT) in pseudopotential plane-wave formalism, as implemented in the Quantum ESPRESSO package [42]. The atomic positions and lattice constants for $1T'$ -WTe₂ are optimized by using Perdew-Burke-Ernzerhof (PBE) [43] functional, and the cutoff energy of 40 Ry and 400 Ry ($1\text{Ry} \approx 13.6\text{eV}$) for the wave functions and the charge density, respectively. A vacuum spacing $\sim 13\text{\AA}$ is used to prevent the interaction between the WTe₂ monolayers. A set of $24 \times 12 \times 1$ k -point sampling is used for Brillouin Zone (BZ) integration over electronic states, and a set of $8 \times 4 \times 1$ q -point grid is used for the phonon calculations to obtain the dynamic matrices. The self-consistent solution of the Kohn-Sham equations is obtained when the total energy changed by less than 10^{-8} Ry and the Hellmann-Feynman force on each atom is less than 10^{-6} Ry/bohr ($1\text{bohr} \approx 0.529177\text{\AA}$). The lattice constants thus are determined with $a_0 = 3.49\text{\AA}$ and $b_0 = 6.31\text{\AA}$ and agree with the experimental [14, 44] and theoretical [13, 17] values.

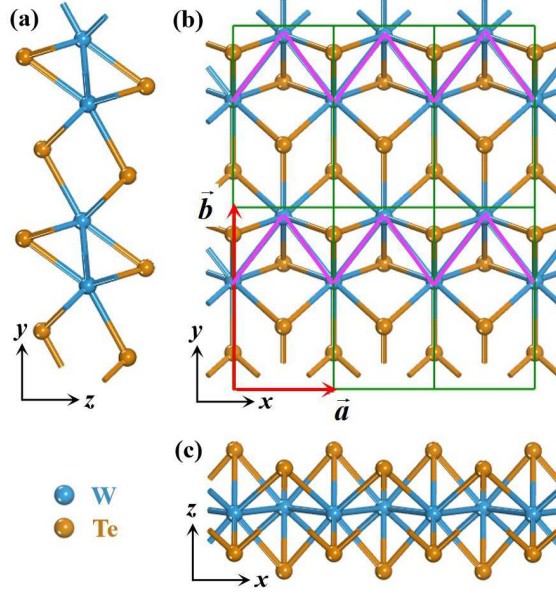


FIG. 1: (color online) Crystalline structure of monolayer $1T'$ -WTe₂ with (a) side view, (b) top view and (c) front view. The distorted W atoms form one-dimensional zigzag chains indicated by the pink lines. The primitive cells (green rectangles) and the primitive vectors a and b (red arrows) used in the calculations are shown in (b).

III. RESULTS AND DISCUSSION

The primitive cell of $1T'$ -WTe₂ is indicated by green rectangle, and its primitive vectors, \vec{a} and \vec{b} , are indicated by red arrows as shown in Fig. 1(b). Along a -axis direction, the distorted W atoms form 1D zigzag chains indicated by the pink lines. In the W - W chains as shown in Fig. 1(c), the stress (corresponding to $E_{bb} = 110.14 \text{ N/m}$) is larger than one in the b axis as shown in Fig. 1(a), based on our calculation of Young's modulus matrix $E = \begin{pmatrix} 78.59 & 27.68 \\ 28.43 & 110.14 \end{pmatrix} \text{ N/m}$ which are in agreement with the theoretical [18] and experimental [34] values. Due to the stronger bond strength in W - W chains, one can expect that $1T'$ -WTe₂ could withstand larger strain along the a -axis direction compared to the b -axis direction. These two directions are the subject of our study. A state of uniaxial strain along a -axis and b -axis is constructed by applying the nominal strain and , respectively, where a and b are the strained lattice constants of $1T'$ -WTe₂.

To obtain the phonon and Raman spectra of strained $1T'$ -WTe₂, we firstly calculate the phonon dispersion curves of intrinsic one, and then analyse the characteristics of Raman-

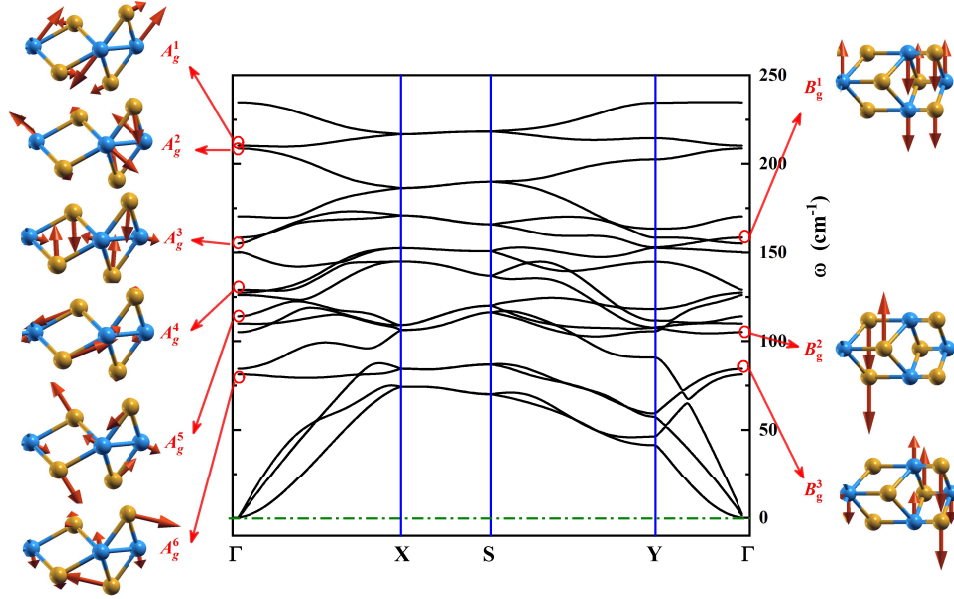


FIG. 2: (Color online) Calculated phonon dispersion relations and atomic vibration displacements with their corresponding irreducible representations for nine typical Raman-active modes (marked by the red circles at Γ) in monolayer $1T'$ -WTe₂. Six A_g modes with atoms vibrating in bc plane are listed on the left panel, and three B_g modes with atoms vibrating in ab plane are listed on the right panel. The q point labels Γ, X, S, Y correspond to $(0,0), (1/2,0), (1/2,1/2), (0,1/2)$, respectively, in fraction of the reciprocal lattice vectors.

active modes based on the group theory. As shown in Fig. 2, there exist 18 phonon branches (3 acoustic and 12 optical branches) with 6 atoms (2 tungsten and 4 tellurium) in the primitive cell of $1T'$ -WTe₂. Because monolayer WTe₂ belongs to the No. 11 space group $P21/m$ and the point group C_{2h}^2 , the irreducible representation of the normal modes at Γ point is $6A_g + 3A_u + 3B_g + 6B_u$, in which only 9 modes are Raman-active among 18 phonon modes based on the symmetry analysis of calculated atomic displacements. These nine Raman-active modes as shown in Fig. 2 are $6A_g + 3B_g$, whose frequencies are shown in Table I with other theoretical [31, 32, 35, 45] and experimental counterparts [31–35]. Typical Raman spectrum of $1T'$ -WTe₂ exhibits three prominent Raman peaks at $\sim 210\text{cm}^{-1}$, 160cm^{-1} , and 130cm^{-1} denoted as A_g^1 , A_g^3 and A_g^4 , respectively. Later, we will focus our work exclusively on these three Raman-active modes.

Owing to strongly anisotropic mechanical properties of $1T'$ -WTe₂, we expect that the

three Raman-active modes exhibit diverse characteristics for WTe₂ under different-direction tensions. Therefore, we then calculate the phonon dispersion relations of strained monolayer WTe₂ along a -axis, b -axis as well as ab -biaxis direction, respectively. Interestingly, as red curves shown in Fig. 3, the phonon branches become soft and their frequencies become negative at special q points under different critical strains. For example, when the tensile strain along a -axis direction approaches 11.55% ($\varepsilon_a = 11.55\%$), one of the acoustic modes of 1T'-WTe₂ becomes imaginary near S point indicating structural instability, which consists with Torum's ($\sim 11\%$) [17] and Xiang's ($\sim 12.5\%$) [18] phonon spectra. In particular, applying strains along b -axis direction, Torun *et al* [17] found that the strain-stress curve reaches a maximum at the critical strain of 15% (but without supporting phonon dispersion curves), and Xiang *et al* [18] found that a phonon branch becomes unstable near the Γ point (not pronounced) at the critical strain $\varepsilon_b = 12\%$. However, different from these two works, our study of tensile strain along b -axis direction shows that the ideal strength of monolayer 1T'-WTe₂ is 7% with the soft mode occurring at Y point exactly, which is smaller than that of WTe₂ along a -axis direction with $\varepsilon_a = 11.55\%$. Such anisotropic phonons might be attributed to the 1D structure formed by the W - W chains. Meanwhile, we also calculate the phonon dispersion curves of 1T'-WTe₂ under uniform biaxial strain, as shown in Fig.

TABLE I: The phonon frequencies of nine Raman-active modes at Γ point for 1T'-WTe₂ from Raman experiments and first-principles calculations. The unit of frequency has been converted to cm^{-1} for direct comparison with the Raman measurements.

symmetry	Exp.[31]	Exp.[32]	Exp.[33]	Exp.[34]	Exp.[35]	Cal.[31]	Cal.[32]	Cal.[35]	Cal.[45]	Cal.(this work)
A_g^1	213.2	217	212	216		222.6	219	221.9	208.9	210.3
A_g^2					216.1	220.3		220.5	208.4	208.7
B_g^1						185.7		173.7	161.3	158.5
A_g^3	161.9	164	165	164	164.3	164.5	168	165.9	156.5	155.1
A_g^4	132.8				135.9	137.2	135	136.9	129.9	128.9
A_g^5					119.7	118.5	119	119.7	114.4	114.1
B_g^2					109.4	108.5		110.4	105.8	105.1
B_g^3				86	88.9	93.2	89	92.5	87.2	84.5
A_g^6			81		85.7	81.4		84.6	80.0	81.4

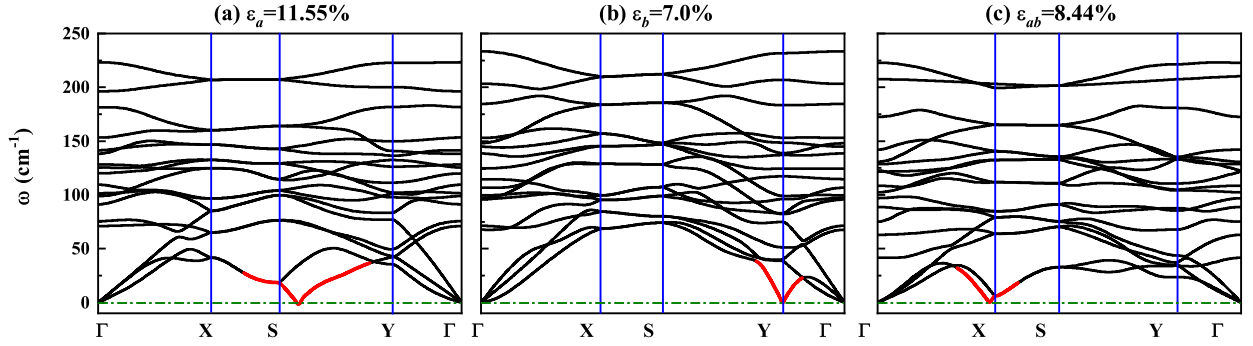


FIG. 3: (Color online) Calculated phonon dispersion relations for monolayer $1T'$ -WTe₂ at different critical strains (a) $\varepsilon_a = 11.55\%$ and (b) $\varepsilon_b = 7.0\%$ uniaxial tension along a and b direction, respectively, and (c) $\varepsilon_{ab} = 8.44\%$ equibiaxial tension. The red phonon dispersion curves show negative-frequency modes (named soft modes) at special q points, indicating the structural instability.

3(c), a soft mode occurs near X point at critical strain $\varepsilon_{ab} = 8.44\%$ indicating a possible phase transition with the $1T'$ -WTe₂ fracture.

Finally, we analyse the response of Raman-active modes (A_g^1 , A_g^3 and A_g^4) on the three direction strains before $1T'$ -WTe₂ rupture. Due to A_g modes containing double-rotation symmetry-axis operation $C_2(z)$ based on the character table for point group C_{2h} , they belong to tangential shear modes with opposite direction vibrations of W - W or Te - Te pairs. Moreover, the vibration displacements of A_g modes (see Fig. 2) are in the bc plane of $1T'$ -WTe₂, perpendicular to the a -axis direction, therefore, one can expect that the effects of a -axis strain on the A_g modes would be weaker than that of b -axis strain. As a result, A_g^4 mode stays relatively unchanged when $1T'$ -WTe₂ under uniaxial strain along a -axis direction, with small slope value of $-0.29\text{cm}^{-1}/\%$, as the red line shown in Fig. 4(c). In order to make the frequency/strain ratio of three modes comparable, we put them in one figure with the same scale of the frequency and strain graduations, respectively. And in Fig. 4, we do find that the frequency shifts in three modes with b -axis strain are all much larger than that with a -axis strain, indicating a clear Raman modes anisotropy. This anisotropic Raman-strain response can facilitate the determination of the crystallographic orientation in $1T'$ -WTe₂. Moreover, when applying biaxial strain to $1T'$ -WTe₂, the frequencies of three

Raman modes also red-shift, but exhibit most sensitive to biaxial strain compared to uniaxial strains, with corresponding largest slope values. To explain this, we plot Figure 5. In Fig.5, one can find that, although the bond angle of W - W chain is almost unchanged when $1T'$ - WTe_2 under equibiaxial strain, the W - W bond length, the vertical distances in two pairs of Te atoms (c_1 and c_2 , respectively) are all dramatically changed compared to the uniaxial strains. This structure modification under biaxial strain, in turn, leads to a considerable change in the Raman-active modes.

For A_g^1 and A_g^4 modes, their frequencies decrease almost linearly with applied strains as shown in Fig. 4(a) and (c), respectively, therefore, the strain in $1T'$ - WTe_2 can be quantified by A_g^1 or A_g^4 mode in Raman spectra. However, for A_g^3 mode, the frequency shift undergoes a sharp turn at about 5% for both uniaxial and biaxial strains, as shown in Fig. 4(b), for example, the calculated biaxial-strain coefficient for A_g^3 mode is down from $-2.22cm^{-1}/\%$ to $-6.03cm^{-1}/\%$. This redshift transition might be result from that the lattice symmetry is maintained before 5% strains and then broken after 5% strains applied. Because the A_g^3 mode consists of both in-plane and out-of-plane motions as shown in Fig. 2, with regard to the relative motions in pairs of W atoms (in-plane) and pairs of Te atoms (out-of-plane), the parallelogram without W - W chains could maintain its shape, but the parallelogram with W - W chains might be flattened or prolonged. Moreover, the amplitudes of Te atoms are much larger than that of W atoms, especially external strains strengthen the motions of Te atoms but weaken the vibrations of W atoms, which would prompt the symmetry broken at last. So, for this particular A_g^3 transition to external strains and A_g^3 as the most significant peak with the largest intensity in Raman spectra, we hope this phenomena can be tested by future Raman experiments of strained $1T'$ - WTe_2 .

IV. CONCLUSIONS

In conclusion, by using DFT and DFPT simulations, we have systematically obtained the Raman spectrum of monolayer $1T'$ - WTe_2 under tensile strains. Our results demonstrate that A_g^1 , A_g^3 and A_g^4 modes, corresponding to the main peaks in Raman spectra of $1T'$ - WTe_2 , are more sensitive to uniaxial strain along b -axis direction than that along a -axis (containing W - W chains) direction, exhibiting anisotropic Raman-strain response. In particular, biaxial strain induces the largest red-shift of the Raman modes compared to the uniaxial strains.

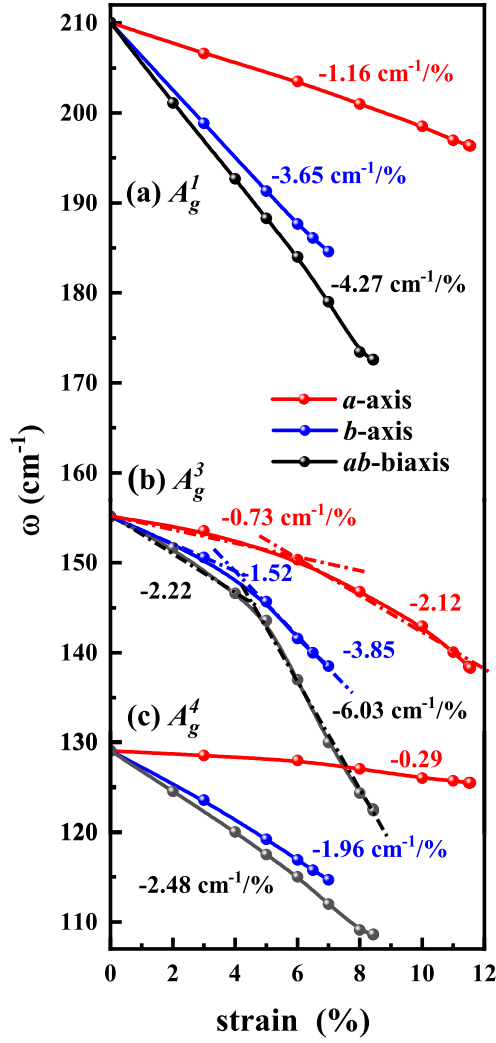


FIG. 4: (Color online) The phonon frequencies of (a) A_g^1 , (b) A_g^3 , and (c) A_g^4 modes (corresponding to three Raman peaks experimentally) versus strains along a -axis (red), b -axis (blue), and ab -biaxial (black) directions, respectively. The solid lines are linear fits to the calculated frequencies (solid symbols) and the corresponding slope values are shown.

Through careful structure configuration analysis, we reveal that the irregularity comes from the dramatic change of the W - W bond length as well as the vertical distances in two pairs of Te atoms under biaxial strain. More interesting, A_g^3 mode undergoes a Raman-shift transition at about 5% for both uniaxial and biaxial strains, different from the A_g^1 and A_g^4 modes whose frequencies show linear dependence on tensile strains. The underlying symmetry rea-

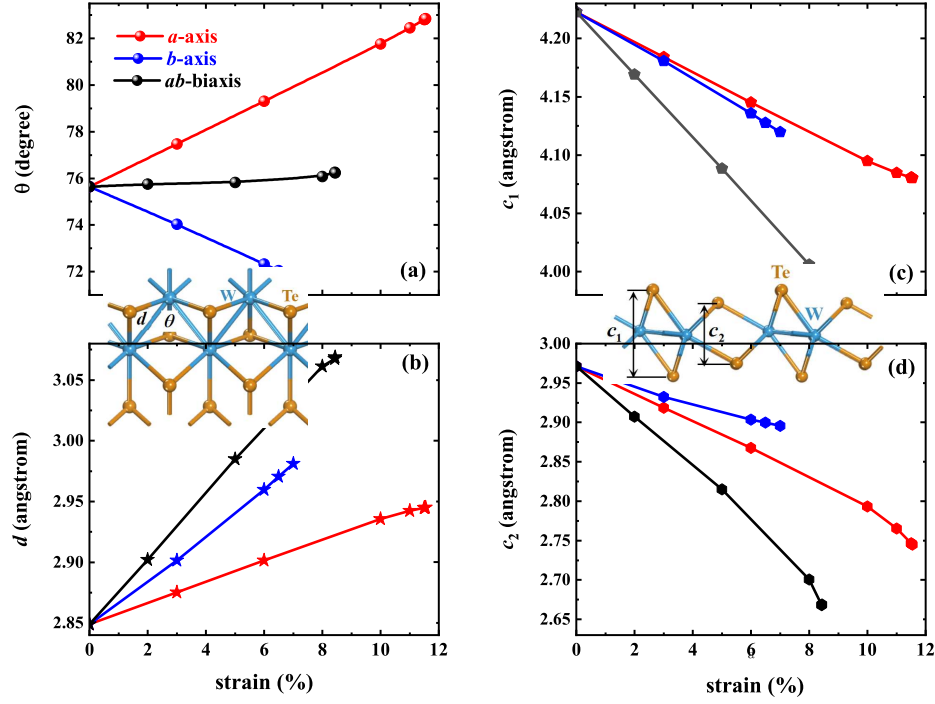


FIG. 5: (Color online) The calculated (a) $W-W-W$ bond angle θ , (b) $W-W$ bond length d , (c) and (d) vertical distance of two pairs of Te atoms in c axis, i.e., c_1 and c_2 , respectively, as functions of a -axis strain (red lines), b -axis strain (blue lines) and biaxial strain (black lines). The inset crystal configurations are used to depict these calculated variables.

son is revealed to be that the competition and cooperation of the relative motions between W -atom pairs and Te -atom pairs modify the shape of $1T'$ -WTe₂. The revealed Raman modes responses to tensile strain are useful for tracing or detecting operations on $1T'$ -WTe₂ based flexible devices.

Acknowledgments

This work was supported by the National Key R&D Program of China under Grant Nos. 2017YFB0403602 and 2016YFB0400603, the National Natural Science Foundation of China

under Grant No. 61605014, and the China PFCAEP under Grant No. YZJLX2016010.

- [1] J. A. Wilson and A. D. Yoffe, *Adv. Phys.*, 1969, **18**, 193-335.
- [2] X. F. Qian, J. W. Liu, L. Fu and J. Li, *Science*, 2014, **346**, 1344-1347.
- [3] F. P. Zheng, C. Y. Cai, S. F. Ge, X. F. Zhang, X. Liu, H. Lu, Y. D. Zhang, J. Qiu, T. Taniguchi, K. Watanabe, S. Jia, J. S. Qi, J. H. Chen, D. Sun and J. Feng, *Adv. Mater.*, 2016, **28**, 4845-4851.
- [4] Z. Y. Jia, Y. H. Song, X. B. Li, K. J. Ran, P. C. Lu, H. J. Zheng, X. Y. Zhu, Z. Q. Shi, J. Sun, J. S. Wen, D. Y. Xing and S. C. Li, *Phys. Rev. B*, 2017, **96**, 041108.
- [5] S. J. Tang, C. F. Zhang, D. Wong, Z. Pedramrazi, H. Z. Tsai, C. J. Jia, B. Moritz, M. Claassen, H. Ryu, S. Kahn, J. Jiang, H. Yan, M. Hashimoto, D. H. Lu, R. G. Moore, C. C. Hwang, C. Hwang, Z. Hussain, Y. L. Chen, M. M. Ugeda, Z. Liu, X. M. Xie, T. P. Devereaux, M. F. Crommie, S. K. Mo and Z. X. Shen, *Nat. Phys.*, 2017, **13**, 683-687.
- [6] Z. Y. Fei, T. Palomaki, S. F. Wu, W. J. Zhao, X. H. Cai, B. S. Sun, P. Nguyen, J. Finney, X. D. Xu and D. H. Cobden, *Nat. Phys.*, 2017, **13**, 677-682.
- [7] Y. H. Song, Z. Y. Jia, D. Q. Zhang, X. Y. Zhu, Z. Q. Shi, H. Q. Wang, L. Zhu, Q. Q. Yuan, H. J. Zhang, D. Y. Xing and S. C. Li, *Nat. Commun.*, 2018, **9**, 4071.
- [8] S. Y. Xu, Q. Ma, H. T. Shen, V. Fatemi, S. F. Wu, T. R. Chang, G. Q. Chang, A. M. M. Valdivia, C. K. Chan, Q. D. Gibson, J. D. Zhou, Z. Liu, K. Watanabe, T. Taniguchi, H. Lin, R. J. Cava, L. Fu, N. Gedik and P. Jarillo-Herrero, *Nat. Phys.*, 2018, **14**, 900-906.
- [9] J. L. Yang, Y. J. Jin, W. P. Xu, B. B. Zheng, R. Wang, and H. Xu, *J. Phys. Chem. Lett.*, 2018, **9**, 4783-4788.
- [10] Y. M. Shi, J. Kahn, B. Niu, Z. Y. Fei, B. S. Sun, X. H. Cai, B. A. Francisco, D. Wu, Z. X. Shen, X. D. Xu, D. H. Cobden and Y. T. Cui, Imaging Quantum Spin Hall Edges in Monolayer WTe₂, 2018, arXiv:1807.09342.
- [11] S. F. Wu, V. Fatemi, Q. D. Gibson, K. Watanabe, T. Taniguchi, R. J. Cava and P. Jarillo-Herrero, *Science*, 2018, **359**, 76-79.
- [12] D. MacNeill, G. M. Stiehl, M. H. D. Guimaraes, R. A. Buhrman, J. Park and D. C. Ralph, *Nat. Phys.*, 2017, **13**, 300-305.
- [13] S. F. Wu, *Bull. Am. Phys. Soc.*, 2018, <https://meetings.aps.org/Meeting/MAR18/Session/B37.4>.

- [14] B. E. Brown, *Acta Crystallogr.*, 1966, **20**, 268–274.
- [15] M. N. Ali, J. Xiong, S. Flynn, J. Tao, Q. D. Gibson, L. M. Schoop, T. Liang, N. Hal-dolaarachchige, M. Hirschberger, N. P. Ong and R. J. Cava, *Nature*, 2014, **514**, 205-208.
- [16] J. H. Wang, W. Yang, M. Zhou, Y. Yang, J. Y. Yan and P. Zhang, *Phys. Lett. A*, 2018, **382**, 2754-2758.
- [17] E. Torun, H. Sahin, S. Cahangirov, A. Rubio and F. M. Peeters, *J. Appl. Phys.*, 2016, **119**, 074307.
- [18] H. Xiang, B. Xu, J. Q. Liu, Y. D. Xia, H. M. Lu, J. Yin and Z. G. Liu, *AIP Adv.*, 2016, **6**, 095005.
- [19] S. K. Deng, A. V. Sumant and V. Berry, *Nano Today*, 2018, **22**, 14-35.
- [20] C. A. Marianetti and H. G. Yevick, *Phys. Rev. Lett.*, 2010, **105**, 245502.
- [21] C. Si, W. H. Duan, Z. Liu and F. Liu, *Phys. Rev. Lett.*, 2012, **109**, 226802.
- [22] W. Yang, Y. Yang, F. W. Zheng and P. Zhang, *Appl. Phys. Lett.*, 2013, **103**, 183106.
- [23] W. Yang, Y. Yang, F. W. Zheng and P. Zhang, *J. Chem. Phys.*, 2013, **139**, 214708.
- [24] S. Horzum, H. Sahin, S. Cahangirov, P. Cudazzo, A. Rubio, T. Serin and F. M. Peeters, *Phys. Rev. B*, 2013, **87**, 125415.
- [25] H. Sahin, S. Tongay, S. Horzum, W. Fan, J. Zhou, J. Li, J. Wu and F. M. Peeters, *Phys. Rev. B*, 2013, **87**, 165409.
- [26] C. R. Zhu, G. Wang, B. L. Liu, X. Marie, X. F. Qiao, X. Zhang, X. X. Wu, H. Fan, P. H. Tan, T. Amand and B. Urbaszek, *Phys. Rev. B*, 2013, **88**, 121301.
- [27] C. H. Chang, X. F. Fan, S. H. Lin and J. L. Kuo, *Phys. Rev. B*, 2013, **88**, 195420.
- [28] Y. L. Wang, C. X. Cong, C. Y. Qiu and T. Yu, *Small*, 2013, **9**, 2857-2861.
- [29] Y. L. Wang, C. X. Cong, W. H. Yang, J. Z. Shang, N. Peimyoo, Y. Chen, J. Y. Kang, J. P. Wang, W. Huang and T. Yu, *Nano Res.*, 2015, **8**, 2562-2572.
- [30] X. Zhang, X. F. Qiao, W. Shi, J. B. Wu, D. S. Jiang and P. H. Tan, *Chem. Soc. Rev.*, 2015, **44**, 2757-2785.
- [31] Y. C. Jiang, J. Gao and L. Wang, *Sci. Rep.*, 2016, **6**, 19624.
- [32] Y. Kim, Y. I. Jhon, J. Park, J. H. Kim, S. Lee and Y. M. Jhon, *Nanoscale*, 2016, **8**, 2309-2316.
- [33] Q. J. Song, H. F. Wang, X. L. Xu, X. C. Pan, Y. L. Wang, F. Q. Song, X. G. Wan and L. Dai, *Rsc Adv.*, 2016, **6**, 103830-103837.
- [34] J. Lee, F. Ye, Z. H. Wang, R. Yang, J. Hu, Z. Q. Mao, J. Wei and P. X. L. Feng, *Nanoscale*,

- 2016, **8**, 7854-7860.
- [35] Y. Cao, N. Sheremetyeva, L. B. Liang, H. Yuan, T. T. Zhong, V. Meunier and M. H. Pan, *2D Mat.*, 2017, **4**, 035024.
 - [36] M. K. Jana, A. Singh, D. J. Late, C. R. Rajamathi, K. Biswas, C. Felser, U. V. Waghmare and C. N. R. Rao, *J. Phys.-Condens. Mat.*, 2015, **27**, 285401.
 - [37] W. D. Kong, S. F. Wu, P. Richard, C. S. Lian, J. T. Wang, C. L. Yang, Y. G. Shi and H. Ding, *Appl. Phys. Lett.*, 2015, **106**, 081906.
 - [38] Q. J. Song, X. C. Pan, H. F. Wang, K. Zhang, Q. H. Tan, P. Li, Y. Wan, Y. L. Wang, X. L. Xu, M. L. Lin, X. G. Wan, F. Q. Song and L. Dai, *Sci. Rep.*, 2016, **6**, 29254.
 - [39] X. L. Ma, P. J. Guo, C. J. Yi, Q. H. Yu, A. M. Zhang, J. T. Ji, Y. Tian, F. Jin, Y. Y. Wang, K. Liu, T. L. Xia, Y. G. Shi and Q. M. Zhang, *Phys. Rev. B*, 2016, **94**, 214105.
 - [40] S. M. Oliver, R. Beams, S. Krylyuk, I. Kalish, A. K. Singh, A. Bruma, F. Tavazza, J. Joshi, I. R. Stone, S. J. Stranick, A. V. Davydov and P. M. Vora, *2D Mat.*, 2017, **4**, 045008.
 - [41] K. A. N. Duerloo, Y. Li and E. J. Reed, *Nat. Commun.*, 2014, **5**, 4214.
 - [42] P. Giannozzi, S. Baroni, N. Bonini, M. Calandra, R. Car, C. Cavazzoni, D. Ceresoli, G. L. Chiarotti, M. Cococcioni, I. Dabo, A. Dal Corso, S. de Gironcoli, S. Fabris, G. Fratesi, R. Gebauer, U. Gerstmann, C. Gougoussis, A. Kokalj, M. Lazzeri, L. Martin-Samos, N. Marzari, F. Mauri, R. Mazzarello, S. Paolini, A. Pasquarello, L. Paulatto, C. Sbraccia, S. Scandolo, G. Sclauzero, A. P. Seitsonen, A. Smogunov, P. Umari and R. M. Wentzcovitch, *J. Phys.-Condens. Mat.*, 2009, **21**, 395502.
 - [43] J. P. Perdew, K. Burke and M. Ernzerhof, *Phys. Rev. Lett.*, 1996, **77**, 3865.
 - [44] C. H. Naylor, W. M. Parkin, Z. L. Gao, H. Kang, M. Noyan, R. B. Wexler, L. Z. Tan, Y. Kim, C. E. Kehayias, F. Streller, Y. R. Zhou, R. Carpick, Z. T. Luo, Y. W. Park, A. M. Rappe, M. Drndic, J. M. Kikkawa and A. T. C. Johnson, *2D Mat.*, 2017, **4**, 021008.
 - [45] J. L. Ma, Y. N. Chen, Z. Han and W. Li, *2D Mat.*, 2016, **3**, 045010